

Structural barriers to complete homogenization and wormholing in dissolving porous and fractured rocks

Tomasz Szawęło^{a,*}, Jeffrey D. Hyman^{b,c}, Peter K. Kang^{d,e}, Piotr Szymczak^{a,*}

^a*Institute of Theoretical Physics, Faculty of Physics, University of Warsaw, Warsaw, 02-093, Poland*

^b*Los Alamos National Laboratory, Earth and Environmental Sciences Division, Los Alamos, 87545, NM, USA*

^c*Department of Geology and Geological Engineering, Colorado School of Mines, Golden, 80401, CO, USA*

^d*Department of Earth & Environmental Sciences, University of Minnesota, Minneapolis, 55455, MN, USA*

^e*Saint Anthony Falls Laboratory, University of Minnesota, Minneapolis, 55455, MN, USA*

Abstract

Dissolution in porous media and fractured rocks alters both the chemical composition of the fluid and the physical properties of the solid. Depending on system conditions, reactive flow may enlarge pores uniformly, widen pre-existing channels, or trigger instabilities that form wormholes. The resulting pattern reflects feedbacks among advection, diffusion, surface reaction, and the initial heterogeneity of the medium. Porous and fractured media can exhibit distinct characteristics—for example, the presence of large fractures can significantly alter the network topology and overall connectivity of the system. We quantify these differences with three network models—a regular pore network, a disordered pore network, and a discrete fracture network—evaluated with a unified metric: the flow focusing profile. This metric effectively captures evolution of flow paths across all systems: it reveals a focusing front that propagates from the inlet in the wormholing regime, a system-wide decrease in focusing during uniform dissolution, and the pro-

*Corresponding author.

Email addresses: t.szawello@uw.edu.pl (Tomasz Szawęło), piotrek@fuw.edu.pl (Piotr Szymczak)

Preprint

Published in International Journal of Rock Mechanics and Mining Sciences (2026).

DOI: 10.1016/j.ijrmms.2026.106431

gressive enlargement of pre-existing flow paths during channelization. The metric shows that uniform dissolution cannot eliminate heterogeneity resulting from the network topology. This structural heterogeneity—rather than just pore-diameter or fracture-aperture variance—sets a fundamental limit on flow homogenization and must be accounted for when upscaling dissolution kinetics from pore or fracture scale to the reservoir level.

Keywords: Pore Network Model, Discrete Fracture Network, Flow Focusing Profile, Dissolution Regime, Heterogeneity

1. Introduction

The flow of reactive fluids through rock induces significant changes in both the fluid composition and the properties of the solid matrix, which affects the transport dynamics within the system. Understanding these processes is essential for a wide range of geological and environmental applications. For instance, the safe disposal of high-level radioactive waste depends on the ability to predict the dominant modes of transport in the reservoir [1, 2]. Likewise, assessing contaminant migration requires understanding how flow is focused, because residence time determines whether a pollutant can be neutralized [3, 4, 5]. In both contexts, transport is tightly coupled to the evolving pore structure: reactive fluid remodels the medium and creates preferential pathways that ultimately control system behavior [6, 7, 8]. In the context of CO₂ sequestration, understanding both micro- and macro-scale behavior is critical for process optimization [9, 10, 11, 12, 13]. Predicting the evolution of flow pathways enables the avoidance of clogging and maximization of mineral replacement [14]. It is therefore evident that elucidating the coupling between flow, transport, and the evolving properties of the reservoir is essential to explain the diversity of structures that emerge from dissolution [15, 16, 17, 18].

A wide body of experimental and numerical work has quantified how dissolution patterns depend on the relative time scales of advection, diffusion, and reaction. In porous media, dissolution experiments have investigated the pore scale behavior [19, 20, 21] and patterns emerging at the core scale [17, 18, 22, 23, 24, 25, 26]. Their findings have been reproduced and extended by multi-scale simulations, from direct numerical models to continuum codes [17, 19, 27, 28, 29, 30, 31, 32]. Four principal dissolution regimes are now recognized: compact, wormholing, channeling, and uniform.

In compact (face) dissolution, the reactant is exhausted almost immediately after entering the sample, and a reaction front advances uniformly across its width [17, 33]. When wormholing occurs, advective instabilities localize flow into a few highly conductive channels that propagate from inlet to outlet [28, 34, 35]. In uniform dissolution, the reactant penetrates the full length of the system, enlarging pores homogeneously [18, 36]. Finally, in the channeling regime, initially existing flow pathways are uniformly enlarged along their entire length [32, 37]. Because the transitions between these regimes are subtle, distinguishing between them requires quantitative analysis of the system evolution [38, 39].

Analogous dissolution phenomena also occur in fractured media, where high-permeability discontinuities channel most of the flow, distinguishing them from conventional porous media. Studies of dissolution in single-fracture systems—using both numerical models and flow-through experiments—have extensively documented aperture growth and channel development. [23, 40, 41, 42, 43, 44, 45]. Similarly to porous media, studies of two-dimensional fracture planes have revealed compact, wormhole, and uniform dissolution regimes, each governed by the interplay of flow, transport, and chemical reactions [28, 46, 47]. Although the coupled flow–transport–reaction equations can be solved directly for idealized one- or two-dimensional fractures, doing so for natural systems with thousands of intersecting fractures—such as karst conduit networks—remains computationally formidable. To address this challenge, researchers employ a hierarchy of different representations: two-dimensional grids of intersecting fractures [41, 48, 49], fully three-dimensional networks with spatially variable apertures [50, 51, 52], and stochastic discrete-fracture-network (DFN) models [53, 54]. DFNs are attractive because they incorporate field-derived statistics of fracture aperture, length, and orientation, bridging single-fracture physics and network-scale heterogeneity while remaining computationally tractable for reactive-transport simulations [55].

Porous media and fractured media exhibit fundamentally different physical structures and flow behaviors—fractures, for instance, can generate long-range, highly connected flow pathways—yet the impact of these distinct forms of heterogeneity on dissolution dynamics remains poorly understood and has not been systematically compared. Early work on variable-aperture fractures showed that the volume of reactant required for breakthrough varies non-monotonically with the magnitude of the initial aperture variation; a critical level of heterogeneity minimizes the breakthrough volume [46, 56].

The same trend was reproduced in numerical analysis of porous media that imposed spatially correlated porosity fields [57, 58, 59]. Follow-up studies examined the role of heterogeneity length scale [59] and suggested that the strong heterogeneity–wormholing link observed in small domains diminishes in larger systems [60]. There is, however, agreement that heterogeneity controls competition among channels and promotes tip branching during worm-hole growth [56, 60].

The interplay between heterogeneity and evolving dissolution patterns strongly affects the hydraulic properties of a medium. Pore-network simulations show that uniform dissolution can eliminate all variability in pore diameters [36, 61], whereas dissolving an initially homogeneous medium can instead generate pronounced heterogeneity; these opposing outcomes, in turn, remove or create anomalous transport behavior [6, 61, 62]. Heterogeneity in porous media has also been shown to affect the onset of preferential flow [26, 37, 63], permeability evolution [64], mixing [65], and even the overall dissolution regime [32, 39, 66]. These results show that significant changes in system dynamics can arise solely from adjusting pore-diameter variability. Beyond pore-size variability, heterogeneity also stems from the topology and geometry of pore or fracture networks—specifically, differences in connectivity and in segment-length distributions. This structural heterogeneity also shapes system evolution, influencing processes ranging from karst genesis [67] to mineral carbonation [68].

In this paper, we quantify how different forms of heterogeneity couple with dissolution across a range of flow and reaction conditions. Three network models are analyzed: a regular pore network with variance in pore diameters, a disordered pore network with variance in pore diameters and lengths, and a discrete fracture network with variance in fracture apertures, lengths, and connectivity. We distinguish three heterogeneity types: conduit-scale (pore diameter or fracture aperture), segment-scale (length), and network-scale (connectivity). Tracking each scale through time shows that initial heterogeneity shapes the evolution of flow pathways and ultimately limits the degree to which dissolution can homogenize the system.

2. Reactive Transport in Network Models

We quantitatively describe the dissolution regimes and analyze their transport properties by utilizing network models. We use a capillary pore network model for the dissolving porous medium [17, 31] and a graph representation

of a discrete fracture network for dissolving fractures [53, 54]. We adjust the initial properties, that is, connectivity, lengths of connections, and distributions of pore diameters and fracture apertures, to exhibit the differences in dissolution arising from the structure of the medium.

2.1. Network Generation

We investigate dissolution dynamics in three contrasting network geometries.

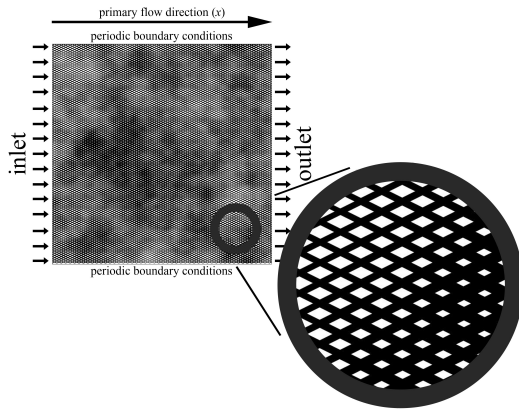
1. Regular pore network – a diamond lattice in which every connection has identical length; variability arises solely from the log-normal distribution of pore diameters (conduit-scale heterogeneity).
2. Disordered pore network – a Delaunay network whose nodes are randomly positioned, introducing heterogeneity in pore lengths and intersection angles while retaining the same diameter distribution as the regular lattice (conduit- and segment-scale heterogeneity).
3. Discrete fracture network – a semi-generic model loosely based on the fractured carbonate-hosted Pietrasecca Fault in the central Apennines, Italy [69]; node locations, fracture intensities, and aperture statistics reproduce the multiscale heterogeneity of natural carbonate fractures (conduit-, segment-, and network-scale heterogeneity).

Figure 1 shows a representative example of each network.

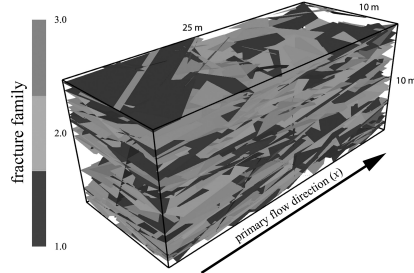
For every geometry we generate 30 statistically equivalent realizations. In the two pore network cases we use a domain of side length L discretized into 100×100 nodes; periodic boundaries are applied perpendicular to the imposed pressure gradient. For the regular pore network, each realization shares the same connectivity but draws pore diameters from an independent log-normal distribution with mean d_0 , variance d_0^2 (that is, the coefficient of variation is ~ 1), and correlation length of $0.1L$; the sampling procedure follows [39, 60]. For the disordered pore network, the nodes are randomly distributed on the domain and connected using Delaunay triangulation; node positions are different for each realization. Pore diameters are assigned from the same distributions as for the regular network.

The DFN domain ($25 \text{ m} \times 10 \text{ m} \times 10 \text{ m}$) is populated with three fracture families that differ in orientation, length distribution, aperture statistics, and intensity; full generation parameters are listed in Appendix A. Importantly, each fracture family has a set aperture, constant throughout the realizations,

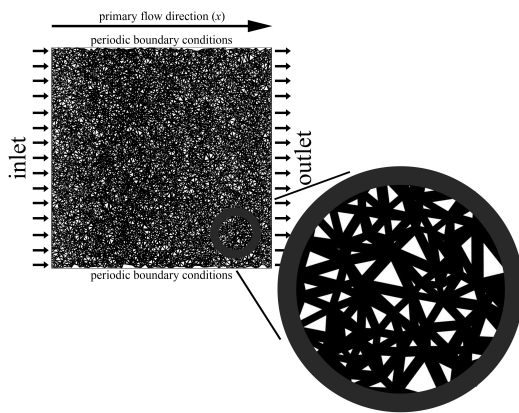
(a) regular pore network



(c) discrete fracture network



(b) disordered pore network



(d) graph representation of DFN

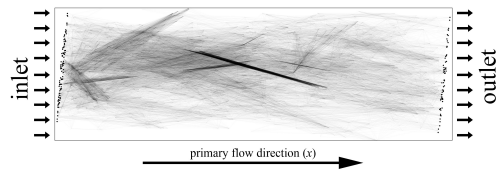


Figure 1: (a) Example regular pore network realization (diamond lattice); edge width is proportional to initial pore diameter. (b) Example disordered pore network realization (Delaunay lattice); edge width again reflects initial pore diameter. (c) Example discrete fracture network; colors denote fracture families. (d) Graph representation of the same DFN, projected into two dimensions via principal-component analysis.

but the proportions between families vary. We convert each DFN to a pipe-network graph with the algorithm of [70], preserving fracture intersections as graph nodes.

In every model the nodes on one boundary serve as the inlet, while those on the opposite boundary form the outlet. In the pore network cases we impose periodic boundary conditions in the direction perpendicular to the inlet–outlet axis.

2.2. Reactive Transport

Our reactive transport model follows the derivations of [31] for pore networks and [71] for single fractures. Volumetric flow q in each channel obeys

$$q = -\frac{C}{\mu}\nabla P, \quad (1)$$

where C is the hydraulic conductance, P the pressure, and μ the fluid viscosity. For a cylindrical pore $C = \pi d^4/128$, with d the pore diameter (Hagen–Poiseuille equation); for a fracture slot $C = wb^3/12$, with w the fracture width and b the aperture (Reynolds equation). A constant total volumetric flow rate Q is enforced by setting $P = P_0$ at the inlet nodes and $P = 0$ at the outlet, then rescaling P_0 at every time step to maintain Q .

A reactant of concentration c_{in} is injected into the inlet nodes. Along each connection we solve the one-dimensional advection–reaction equation

$$q\frac{dc}{dx} = -sk_{\text{eff}}c, \quad (2)$$

where x denotes the direction along the channel length, the reactive surface is $s = \pi d$ for pores and $s = 2w$ for fractures, and k_{eff} is the effective reaction rate,

$$k_{\text{eff}} = k/(1 + kd^{\text{h}}/D\text{Sh}), \quad (3)$$

which takes into account the hindering effects of diffusion across the pore diameter or fracture aperture. In Eq. (3), k denotes the reaction rate, D is the diffusion coefficient, and Sh is the Sherwood number [72, 73, 74]. Finally, d^{h} is the hydraulic diameter, equal to d for pores and $2b$ for fractures. The Sherwood number, Sh , depends on reaction rate at mineral surfaces, but the variation is relatively small, for porous media limited by the values $\text{Sh} = 3.656$ and $\text{Sh} = 4.364$ (we approximate it by a constant value, $\text{Sh} = 4$), while in fractured media, from $\text{Sh} = 7.54$ to $\text{Sh} = 8.24$ (we approximate it by $\text{Sh} = 8$).

Mineral dissolution enlarges each conduit according to

$$\partial_t d = \frac{2k_{\text{eff}}(d)}{\nu c_{\text{sol}}}c, \quad \partial_t b = \frac{2k_{\text{eff}}(b)}{\nu c_{\text{sol}}}c, \quad (4)$$

where c_{sol} is the concentration of soluble material and ν accounts for the stoichiometry of the reaction.

System evolution is governed by two dimensionless numbers: the effective Damköhler number, Da_{eff} , measuring the ratio of advective to reactive time scales, and the reaction-diffusion parameter G , characterizing the hindering effects related to diffusion across the channel.

$$\text{Da}_{\text{eff}} = \frac{s_0 k_{\text{eff}}(d_0^{\text{h}})L}{Q}, \quad G = \frac{k d_0^{\text{h}}}{D\text{Sh}}, \quad (5)$$

where s_0 and d_0^{h} are the initial average reactive surface and hydraulic diameter, respectively.

The two dimensionless groups we employ—the effective Damköhler number Da_{eff} and the transport ratio G —quantify the competition of advective, diffusive, and reactive time scales in both porous and fractured media. We define them with the total volumetric flow rate Q rather than a mean velocity, because strong initial flow focusing in discrete fracture networks (DFNs) makes any “average” velocity unrepresentative. This volumetric definition also remains consistent for our pore–network simulations, which share identical width and an equal number of inlet pores, so Q scales directly with the mean pore velocity.

A direct, one-to-one comparison of Da_{eff} between the two systems is nevertheless impossible. In our models a cross-section perpendicular to the main flow contains only 200 conduits in the pore networks but roughly 5000 fracture elements in the DFNs; the vastly different hydraulic cross-sections imply different residence-time distributions even at the same global flow rate Q . Consequently, we treat Da_{eff} as a system-specific control parameter, scanning it separately for pore and fracture networks and then comparing the resulting dissolution regimes rather than matching absolute values.

Simulation time is measured as the normalized dissolved volume, $T = \Delta V_{\text{tot}}/V_0$, where V_0 is the initial pore volume and ΔV_{tot} is the total dissolved volume in the system.

2.3. Flow Focusing Profile

The main tool that we use to determine the evolution of the system is the flow focusing profile [39]. We segment the medium into cross sections

along the main flow direction, x , and in each of them we calculate the flow focusing index, $f_{50\%}$ [38], according to

$$f_{50\%} = \frac{n_X/2 - n_{50\%}}{n_X/2}, \quad (6)$$

where $n_{50\%}$ is the smallest number of pore or fracture connections carrying 50% of the total flow through a given cross section of the medium, and n_X is the total number of pore or fracture connections in that cross section. Calculating the index, $f_{50\%}$, for cross sections along the entire medium, we obtain a profile measuring flow focusing as a function of distance from the inlet at a given time.

3. Results

Each network type exhibits distinct dissolution behavior due to differences in structural organization and type of heterogeneity. For the regular pore network, all connections are of the same length, and only conduit-scale heterogeneity is present, in the form of the distribution of diameters. In the disordered pore network, apart from the conduit-scale heterogeneity, based on the same noise as in the regular network, there is also the segment-scale heterogeneity in the form of distribution of connection lengths and intersection positions. While in the case of porous media, the conduit- and segment-scale heterogeneity can be of the same order of magnitude, their couplings with dissolution are different, with the latter much more persistent. Finally, in the discrete fracture network, the nodes, connections, and apertures are distributed to approximate a real fracture network, introducing heterogeneity across all scales. Fracture families with various apertures introduce the conduit-scale heterogeneity, variance in fracture lengths generates the segment-scale heterogeneity (which in fractures can be much larger than that in apertures), and finally connectivity within the structure creates heterogeneity on the scale of the entire network, as sometimes only a few fractures can span the entire domain.

We simulate the three systems, choosing the dimensionless parameters Da_{eff} and G to explore the standard dissolution regimes: uniform dissolution, channeling, and wormholing. Figure 2 presents the networks evolving in the wormholing regime, alongside the changes of the flow focusing profile. In pore networks, the dissolution regime becomes apparent almost immediately through the emergence of one or a few dominant channels. In the DFN

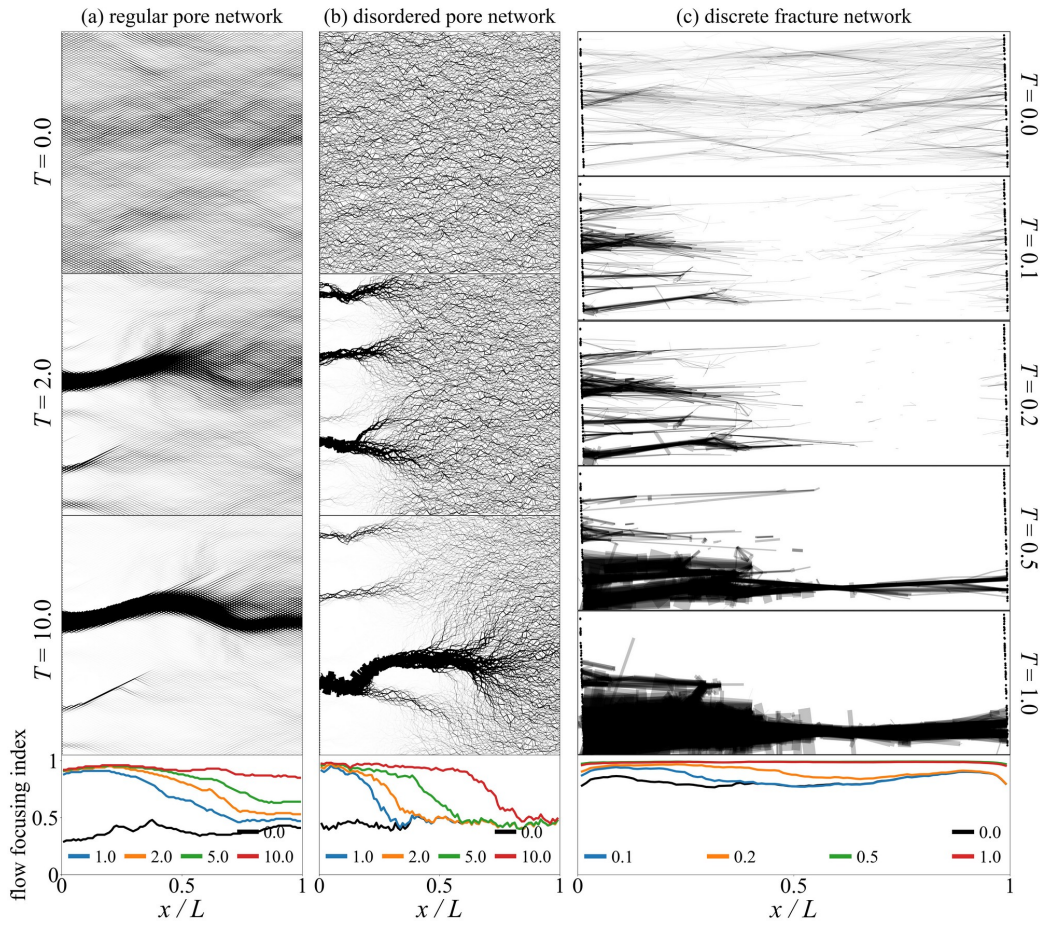


Figure 2: Evolution of the three network types in the wormholing regime. (a) Regular pore network. (b) Disordered pore network. For both pore lattices, edge width is proportional to the volumetric flow rate. (c) Discrete fracture network shown as a graph after a principal-component-analysis projection; edge width scales with flow, but only edges carrying more than 1% of the maximum flow rate in the system are plotted.

the pattern is subtler—flow is further concentrated along pre-existing high-conductivity paths—but a newly developed high-permeability flow path can still be discerned. In each case the dissolution dynamics are captured by the flow focusing profile, which appears as a front of increased focusing that advances from the inlet toward the outlet; this increase is less pronounced in the DFN because strong focusing already exists at $T = 0$.

Because we define the profile in the same way for every network, it acts as a single quantitative metric for both porous and fractured media. Tracking its evolution in (Da_{eff}, G) space lets us compare dissolution in DFNs with that in regular and disordered pore networks, exposing both shared regimes and geometry-specific differences.

3.1. Regular Pore Network

We simulate the regular pore network for $Da_{\text{eff}} \in \{0.002, 0.02, 0.2\}$ and $G \in \{0.1, 1, 5\}$. The flow focusing profile is recorded at $T \in \{0, 1, 2, 5, 10\}$, giving a complete history of the dissolution process. Figure 3 presents the evolution of the network in the three dissolution regimes and Figure 4 shows the profile evolution for each (Da_{eff}, G) pair: panel (a) displays the full range to reveal overall trends, whereas panel (b) focuses on the range of evolution of the profile, containing additional information on variability within the ensemble.

In the uniform regime the flow focusing profile declines with time. The drop is steepest at high G : diffusion hindrance suppresses the growth of the widest channels, allowing narrower ones to dissolve faster so the network approaches complete homogeneity (profile values tend toward zero). At low G the values of the profile also decrease, but now because all channels enlarge at nearly the same rate, reducing their conductance contrasts. A small inlet–outlet asymmetry persists, indicating that the reactant penetration length—though large—is still finite relative to the system length.

In the channeling regime, profile values increase in time along the entire system length. Initial main flow pathways widen almost uniformly from inlet to outlet, although the region near the inlet remains slightly more homogeneous, as more dissolution occurs there before the main flow pathway dominates the system. The effect of G is subtler. At low G the focusing weakens with depth, whereas at high G this decline nearly disappears, because diffusion hindrance allows more reactant to reach the deeper portions of the network. Conversely, at higher G the homogenization near the inlet is more pronounced, as dissolution in smaller channels is then faster.

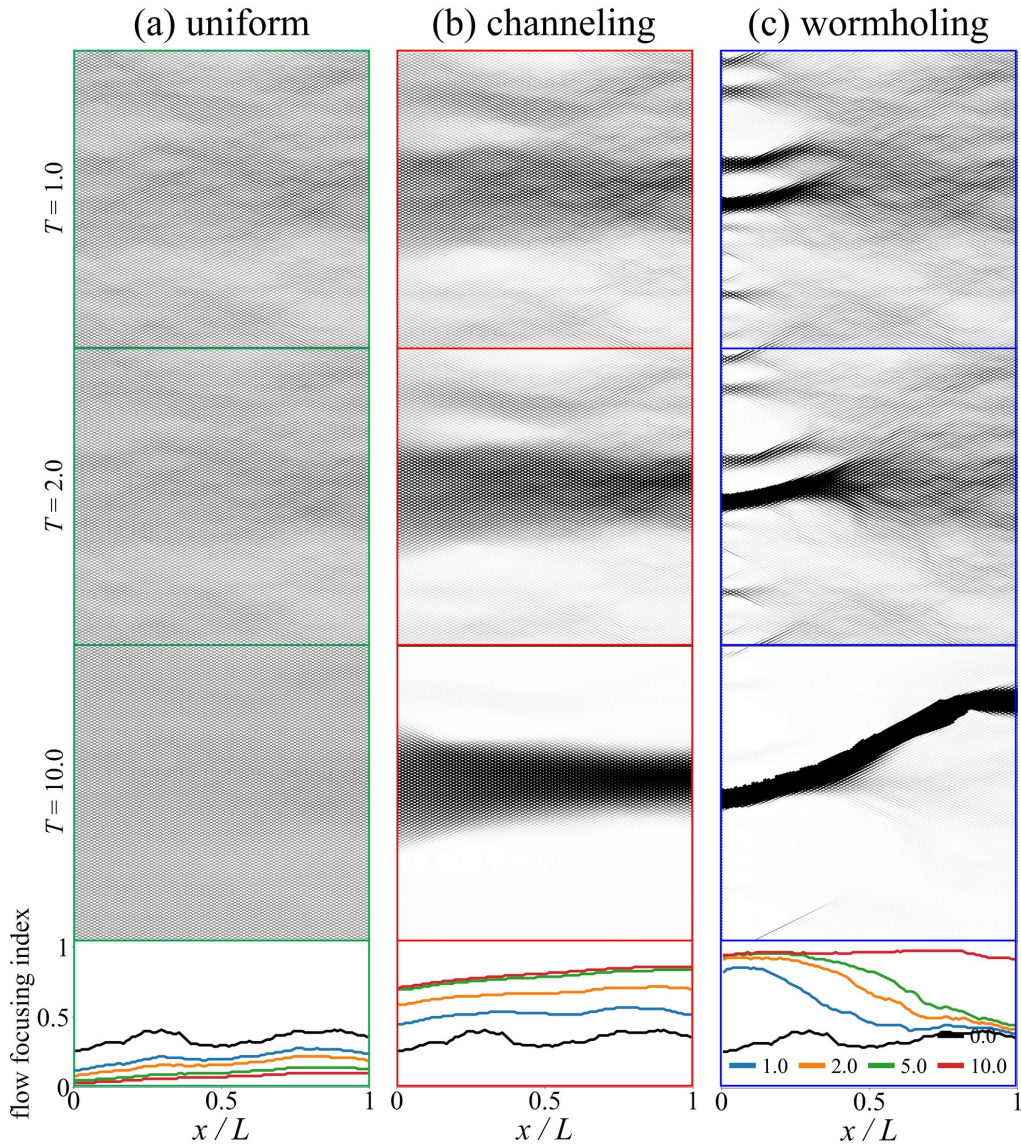


Figure 3: Evolution of the regular pore network and the flow focusing profile in three dissolution regimes: (a) uniform ($Da_{\text{eff}} = 0.002$, $G = 5$), (b) channeling ($Da_{\text{eff}} = 0.02$, $G = 5$), and (c) wormholing ($Da_{\text{eff}} = 0.2$, $G = 5$). Edge width is proportional to the volumetric flow rate.

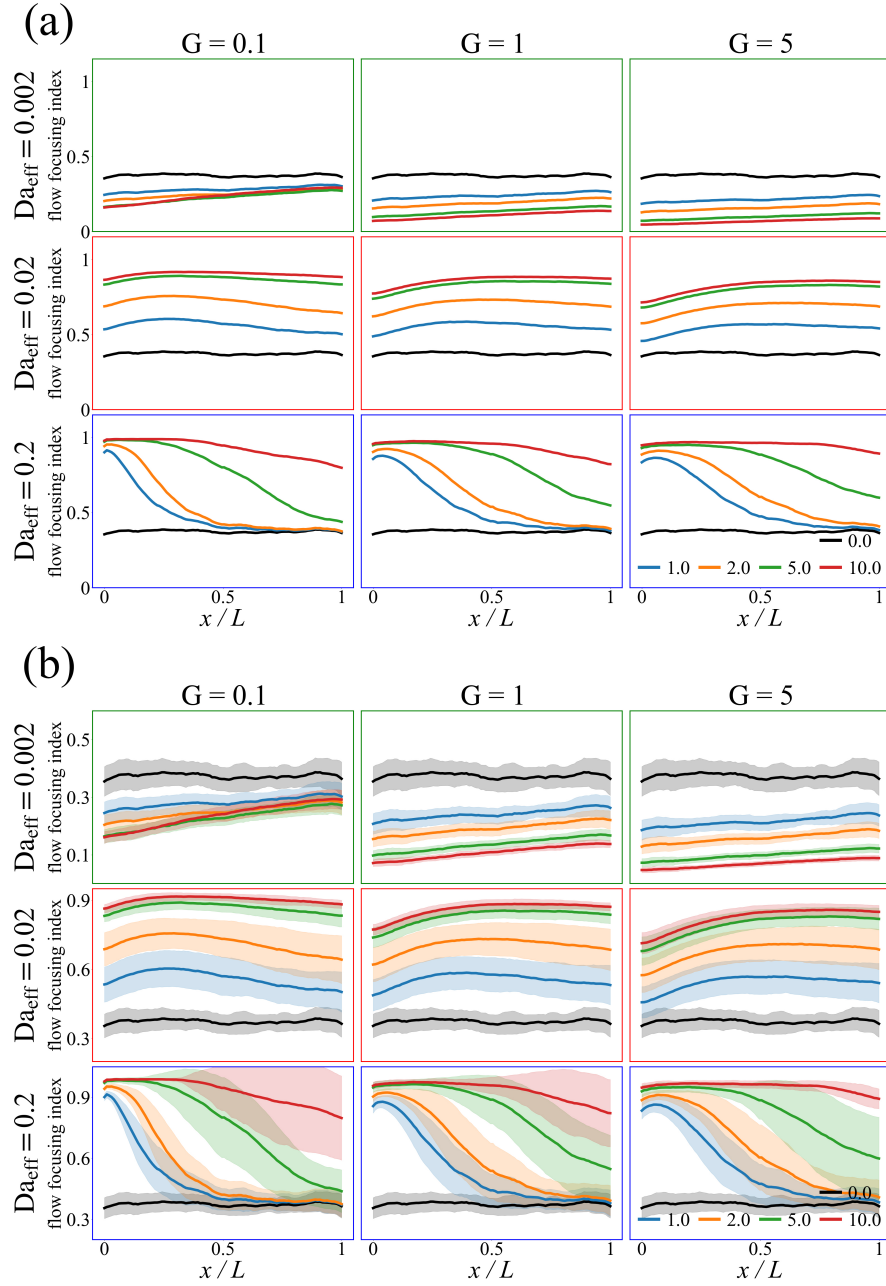


Figure 4: Evolution of the flow focusing profile for the regular pore network across the (Da_{eff}, G) parameter space. (a) Mean profile value at successive time snapshots (solid lines). (b) Same data, with ensemble variability: the shaded band around each curve denotes the mean ± 1 standard deviation across all realizations.

In the wormholing regime, a single highly conductive channel advances through the lattice, producing a sigmoidal profile: near-maximum values behind the tip and unchanged values ahead of it. The progress of the wormhole is faster for larger G —again, due to diffusion hindrance, more reactant is pushed toward the tip of the wormhole, instead of being used for widening the already existing parts of the channel.

Figure 4b shows the variability of the flow focusing profile within the ensemble. The data indicate that, although different network realizations—which vary in their initial pore-diameter distributions—evolve at different rates, the variance becomes negligible by the end of the simulation. This convergence implies that the ultimate outcome—whether the degree of homogenization in the uniform regime or a characteristic level of channelization—does not depend on the specific initial diameter distribution.

3.2. *Disordered Pore Network*

The results of dissolution for the disordered pore network are depicted in Figures 5 and 6. They are in agreement with our previous work [39]. We run the same set of simulations as for the regular lattice, using identical dimensionless parameters. We utilize the same diameter distributions, yet the initial flow focusing index in the ensemble is higher ($f_{50\%} \approx 0.5$ versus 0.4). This difference reflects the additional segment-scale heterogeneity introduced by non-uniform pore lengths and connectivity.

The dissolution patterns evolve at different rates in the disordered and regular pore networks. In the channeling and wormholing regimes, the disordered network advances more slowly: at the same nondimensional time T , the channels in the disordered network extend noticeably less than those in the regular lattice. In the uniform regime, however, the disordered lattice dissolves at a comparable rate—and, at high G , even faster—than the regular network.

Several factors contribute to the contrasting evolution of the two networks. Geometrically, the disordered lattice contains numerous connections perpendicular to the main pressure gradient. These cross-flow channels are nearly inactive in the uniform regime, where transverse pressure differences are negligible, but they start to carry substantial flow once wormholes form, because the wormhole tips impose strong lateral pressure gradients. This is increasing the reactant demand and slowing the growth. Second, pronounced aperture and length heterogeneity promotes branching, which further retards wormhole advance [56, 60]. When heterogeneity becomes extreme, however,

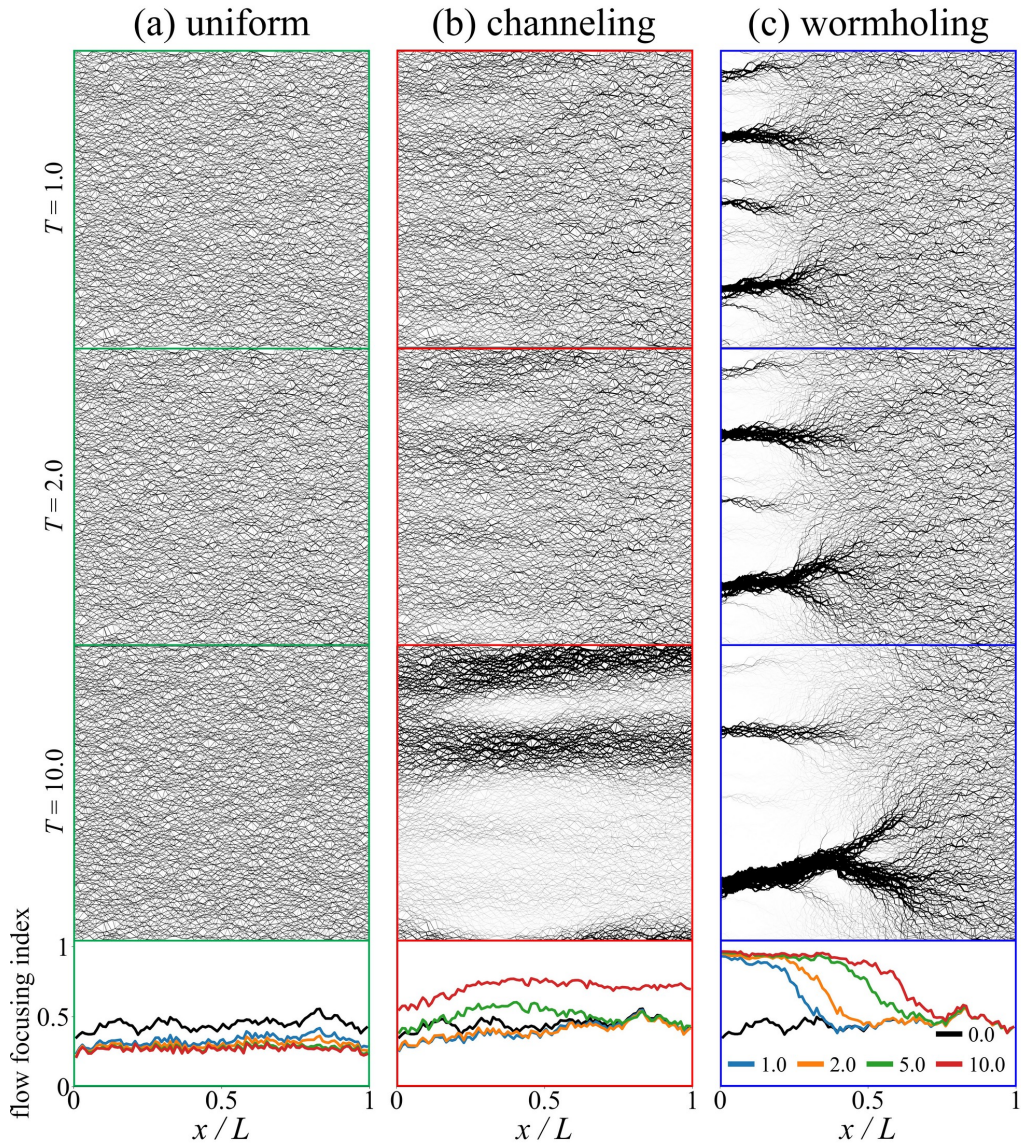


Figure 5: Evolution of the disordered pore network and the flow focusing profile in three dissolution regimes: (a) uniform ($Da_{\text{eff}} = 0.002$, $G = 5$), (b) channeling ($Da_{\text{eff}} = 0.02$, $G = 5$), and (c) wormholing ($Da_{\text{eff}} = 0.2$, $G = 5$). Edge width is proportional to the volumetric flow rate.

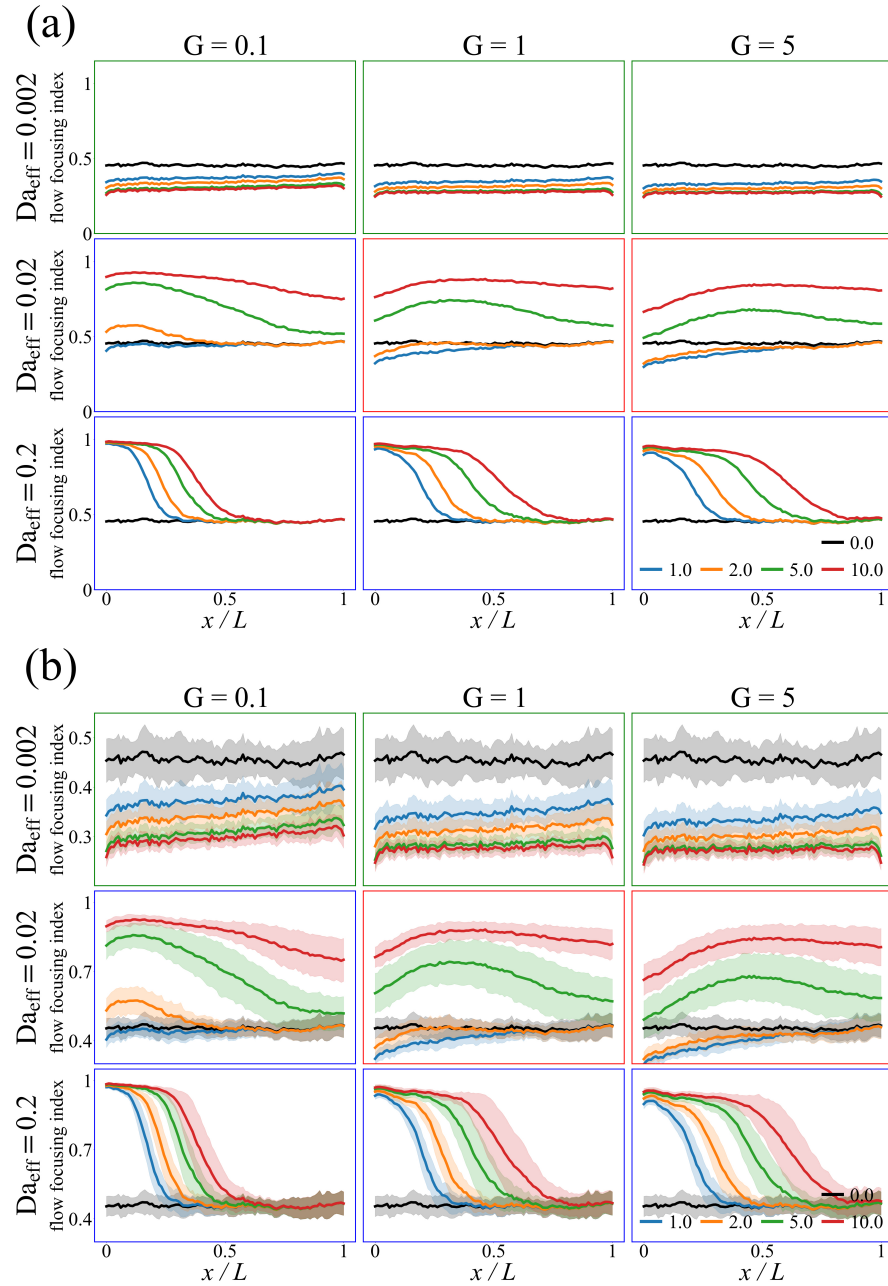


Figure 6: Evolution of the flow focusing profile for the disordered pore network across the (Da_{eff}, G) parameter space. (a) Mean profile value at successive time snapshots (solid lines). (b) Same data, with ensemble variability: the shaded band around each curve denotes the mean ± 1 standard deviation across all realizations.

stronger flow focusing can compensate for the branching penalty and accelerate growth again [56]. Because our disordered network displays significant heterogeneity at both conduit and segment scales, pinpointing its exact position on this spectrum—and how these competing effects balance—remains challenging.

The two networks differ not only in how quickly they evolve but also in how completely they can homogenize. At low Damköhler numbers the disordered network still enters the uniform–dissolution regime, yet the resulting homogenization is weaker than in the regular network. Structural heterogeneity—independent of diameter variations—persists, and even at high G the flow–focusing index plateaus at $f_{50\%} \approx 0.25$. This saturation indicates an intrinsic limit to homogenization in the disordered medium. The snapshots in Fig. 5 change only marginally over time, confirming that much of the initial flow distribution is related to the disordered geometry of the network. This finding is crucial for studies aiming at complete homogenization: although uniform dissolution can eliminate all diameter-based heterogeneity in regular lattices [36, 61], it cannot remove heterogeneity rooted in the network topology. Because natural rocks are never perfectly regular—both pore diameters and lengths vary—results derived from regular pore networks cannot be generalized directly to real systems.

At intermediate Da_{eff} the disordered network behaves differently from the regular lattice. Its extra heterogeneity—especially the variation in pore lengths—impedes the formation of dominant flow pathways spanning the entire system. Figure 5 shows that preferential channels exist from the outset, but they are far less pronounced than in the regular network. This is because the pore-diameter field is spatially correlated and thus encourages channel formation. Clusters of large-diameter pores create contiguous low-resistance corridors, so flow concentrates along them and dissolution amplifies the contrast, sharpening the channel. By contrast, the uncorrelated distribution of pore lengths work against sustained pathway development. As a result, the regime depends strongly on G . At small G , the network displays the features of the wormholing regime: a sigmoidal flow focusing profile and a dominant pathway that grows gradually from inlet to outlet. At higher G , the profile resembles that of the regular network, but with more initial homogenization. Because channel growth is slower, dissolution has more time to smooth out inlet-region heterogeneity before a single path takes over.

At high Da_{eff} both networks consistently develop wormholes and their growth accelerates with increasing G . The key difference lies in how strongly

the wormholes compete. In the regular lattice, screening is stronger, so one wormhole soon outcompetes its neighbors and captures nearly the entire discharge. Once this conduit monopolizes the flow, the high velocity within it increases the reactant penetration length, broadening the transition zone in the flow focusing profile. In the disordered network, weaker screening allows several channels to share the flux; the dominant wormhole advances more slowly, and the focusing profile remains steeper.

The ensemble variability shown in Figure 6b is of the same order of magnitude as in the regular network, but—because it now reflects spatially correlated diameter heterogeneity and the randomness of node positions—the profile is less smooth. How this variability evolves depends on the dissolution regime. In the uniform regime it decreases as conduit-scale heterogeneity is removed. In the channeling regime it first increases and then declines, indicating different evolution rates for individual realizations that eventually converge to a common outcome. In the wormholing regime variable growth rates are also evident; however, because the simulation ends before wormhole breakthrough, the expected late-time reduction in variability is not yet observed.

3.3. Discrete Fracture Network

Figure 7 presents the evolution of the dissolving DFNs and Figure 8 depicts the corresponding changes in the flow focusing profile across the parameter space. We perform the simulations for $Da_{\text{eff}} \in \{0.0002, 0.002, 0.02\}$ and $G \in \{0.1, 1, 5\}$, and capture data at $T \in \{0, 0.1, 0.2, 0.5, 1\}$. The initial values of the flow focusing index are very high ($f_{50\%} \approx 0.8$), indicating that the network is strongly channelized even before any reaction occurs. Because the discrete fracture network has a much larger hydraulic cross-section than the pore lattices, the effective Damköhler numbers required to traverse the three dissolution regimes are shifted roughly one order of magnitude lower. After accounting for this shift, the expected progression—uniform dissolution, channeling, and finally wormholing—emerges unchanged.

In the uniform regime the flow focusing profile shows a modest decrease, maximally to around $f_{50\%} \approx 0.7$, but the values remain high, showing that uniform aperture growth cannot eliminate heterogeneity rooted in fracture connectivity and pathway lengths, making complete homogenization unattainable in a DFN.

In the channeling regime the flow focusing profile rises only slightly with time, as expected for a network that is already strongly channelized. Its

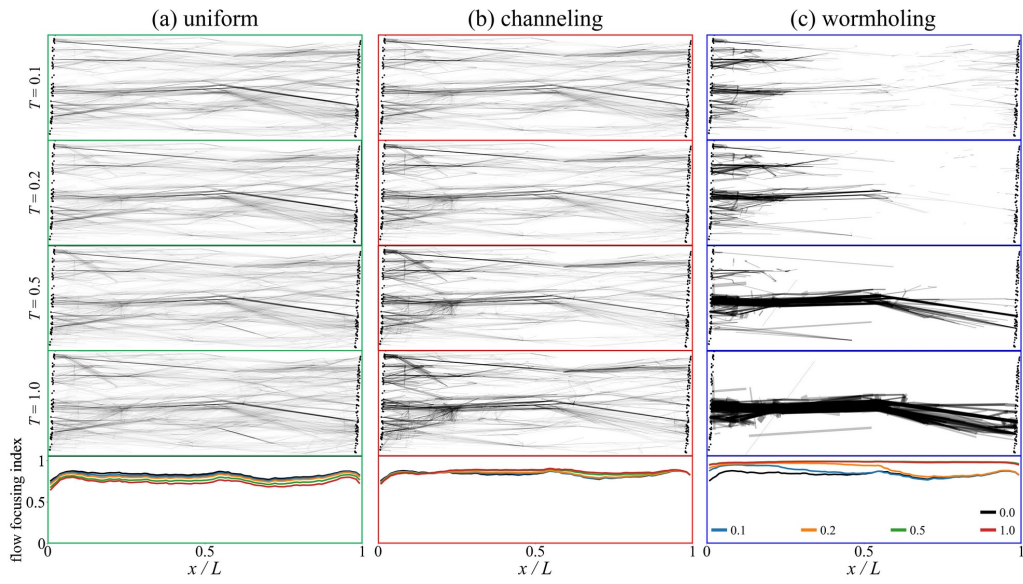


Figure 7: Evolution of the discrete fracture network and the flow focusing profile in three dissolution regimes: (a) uniform ($Da_{\text{eff}} = 0.0002$, $G = 5$), (b) channeling ($Da_{\text{eff}} = 0.002$, $G = 5$), and (c) wormholing ($Da_{\text{eff}} = 0.02$, $G = 5$). The network is shown as a graph after a principal-component-analysis projection; edge width scales with flow, but only edges carrying more than 1% of the maximum flow rate in the system are plotted.

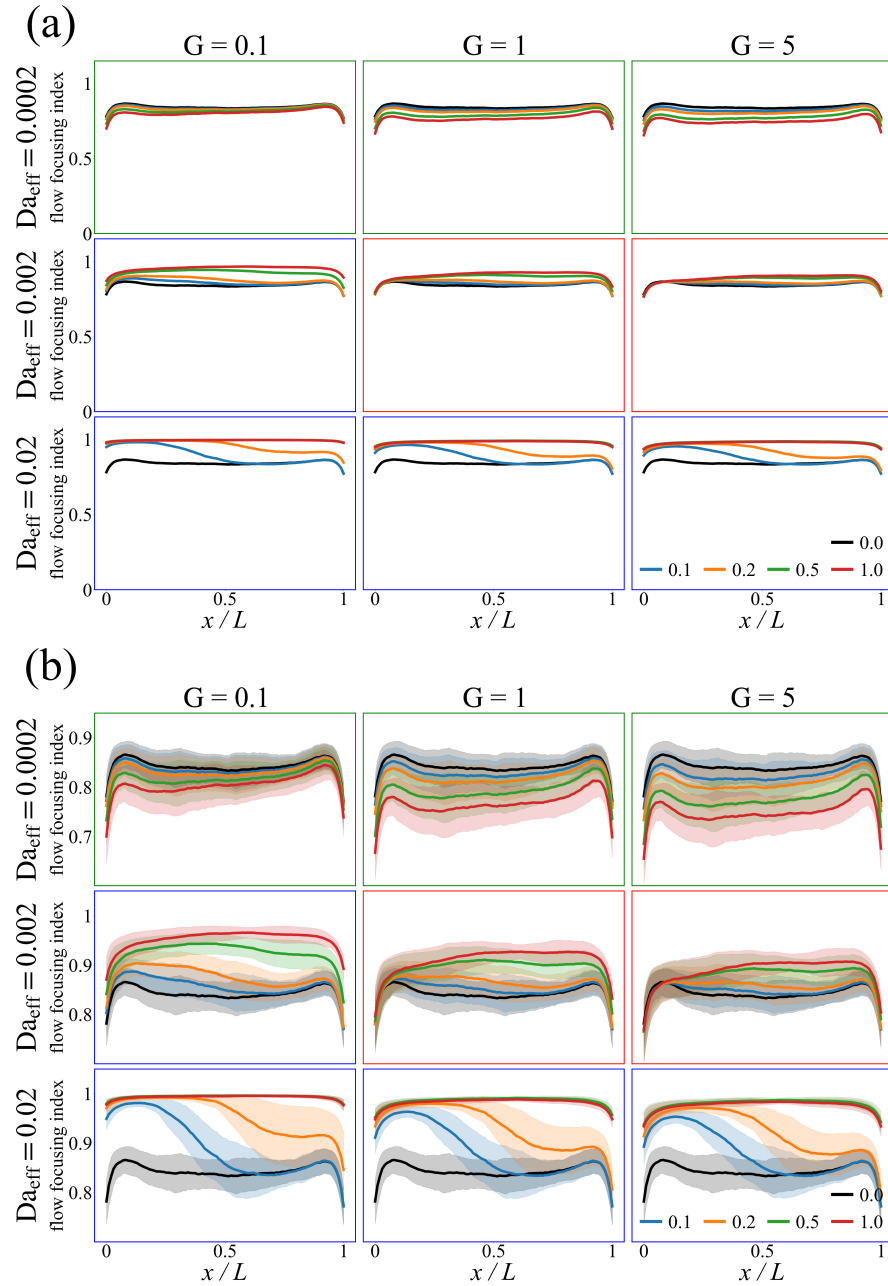


Figure 8: Evolution of the flow focusing profile for the discrete fracture network across the (Da_{eff}, G) parameter space. (a) Mean profile value at successive time snapshots (solid lines). (b) Same data, with ensemble variability: the shaded band around each curve denotes the mean ± 1 standard deviation across all realizations.

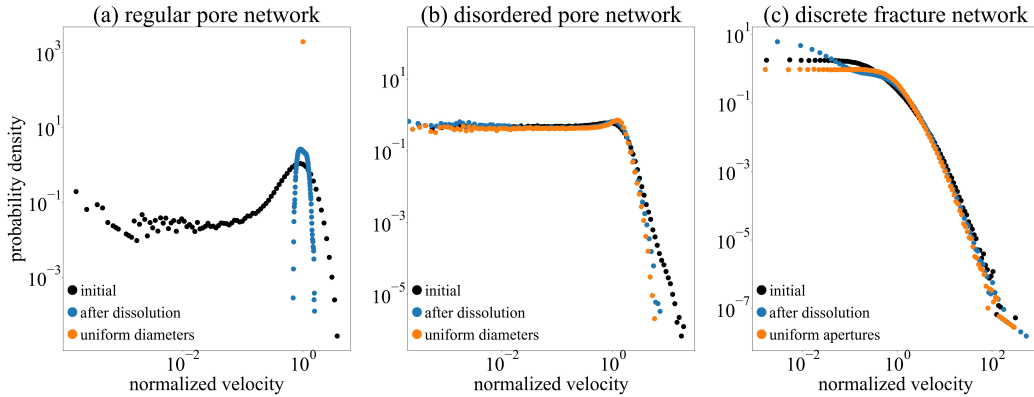


Figure 9: Velocity distributions for three network types: (a) regular pore network, (b) disordered pore network, and (c) discrete fracture network. Each panel contains three histograms: initial distribution, after uniform dissolution, and the distribution for the same ensemble, but with uniform diameters or apertures. Velocities are normalized by the ensemble-average velocity in each case.

shape, however, evolves much like in porous media: the increase is nearly uniform across the entire domain. In addition, for $Da_{\text{eff}} = 0.002$ and $G = 0.1$, the DFN transitions to the wormholing regime, mirroring the behavior of the disordered pore network and further underscoring the influence of additional heterogeneity.

In the wormholing regime the flow focusing profile develops a transition zone, much like in porous media. A notable difference, however, is that a higher G slows wormhole advance—the opposite of the behavior seen in pore networks. At the same time, the flow focusing index no longer approaches its maximum when G is large. This indicates that diffusion limitation becomes significant, restricting dissolution in the main channel. As a result, competition among flow paths weakens; smaller channels continue to carry a portion of the flux, thereby reducing the growth rate of the dominant pathway.

The variability in the flow focusing index (Figure 8b) mirrors that of the disordered pore network, rising at first and then declining as dissolution proceeds. In the DFNs the wormholes ultimately reach the outlet, and, once breakthrough occurs, the profile exhibits the expected reduction in variability.

3.4. Homogenization by Dissolution

The flow focusing data show that perfect homogenization is unattainable in either disordered porous media or DFNs. To examine why, we compare the velocity distributions for all three network types. Specifically, we sample the initial velocity distribution, the distribution after uniform dissolution (final snapshots for $Da_{\text{eff}} = 0.002$, $G = 5$ in Figures 4 and 6, and $Da_{\text{eff}} = 0.0002$, $G = 5$ in Figure 8), and the distribution for an ideal network with perfectly uniform diameters and apertures.

Figure 9 presents the comparison of these distributions. For the regular pore network, the initial histogram is broad because of diameter variability; after dissolution it narrows sharply and collapses to a single value in the uniform diameter limit. This behavior is consistent with other studies that use the regular pore network [36, 61].

In the disordered network the initial velocity histogram is broad, with a high-velocity tail generated by the largest pores. Uniform dissolution trims this tail by reducing the contrast between large and small pores. At the same time, very low velocities become more common: as heterogeneity diminishes, flow aligns with the main pressure gradient and many pores oriented perpendicular to it carry negligible flux. Interestingly, the histogram after dissolution almost coincides with that of the uniform-diameter lattice, confirming that the remaining heterogeneity—and thus the residual flow focusing index—is rooted in network structure, not in diameter variance.

The DFN follows the same overall trend: the high-velocity tail shortens, and the number of low-velocity fractures increases. After dissolution the tail closely matches the uniform-aperture case, yet the low-velocity end still differs markedly. This mismatch likely results from the three fracture families in the structure of the DFN, which begin with distinct initial apertures. Dissolution broadens the aperture distribution of each family, but not enough for fractures from different families to overlap in large numbers. Forcing all apertures to a single initial value would eliminate this discrepancy—but at the cost of fundamentally altering the structure of the network.

Whether we look at the network after dissolution or at an idealized version with uniform diameters or apertures, the velocity distributions are still far from the delta-like peak achieved by the regular pore lattice. All residual variance is therefore dictated by structural heterogeneity. Because that heterogeneity is greater in the DFN than in the disordered pore network, the lowest attainable flow focusing index is likewise higher. The principle is

the same in every case: once the network geometry sets a structural limit, additional dissolution cannot homogenize the flow any further.

4. Conclusions

Dissolution reshapes both structure and flow in porous and fractured media – systems whose contrasting architectures and transport behaviors influence many geologic and engineering processes. To quantify these effects, we performed network-based simulations on three models: a regular pore network, a disordered pore network, and a discrete fracture network, spanning a wide range of flow and reaction conditions. The results are quantified using the flow focusing profile. Every dissolution regime presents distinct characteristics in each system. In the uniform regime, all networks are homogenized and flow focusing decreases across the entire domain. However, while the flow in the regular medium becomes completely uniform, the disordered medium retains a certain level of focusing, and the discrete fracture network remains highly heterogeneous, with only minimal redirection of flow to the parts of the network beyond the main pathways.

In the channeling regime, we observe an increase in flow focusing along the whole system, with slight inlet–outlet asymmetry in the regular medium and a much more pronounced asymmetry—with significant homogenization near the inlet—in the disordered medium. For the discrete fracture network, this increase is minimal, as the flow is highly channelized from the outset. In the wormholing regime, a front in the flow focusing profile progresses from the inlet, marking wormhole formation, but the speed of the wormhole and the sharpness of the front differ between the systems.

We focused our analyses on the interplay between heterogeneity and uniform dissolution. The three systems exhibited different types and degrees of heterogeneity, and each responded to dissolution in its own way. In the regular network, heterogeneity arose solely from the pore-diameter distribution and was readily eliminated by uniform dissolution. In the disordered network and the DFN, additional structural heterogeneity persisted: the lengths of individual pathways and the connectivity between parts of the network remained unchanged. Uniform dissolution therefore removed only the heterogeneity associated with diameter or aperture variations, demonstrating that the inherent structure exerted strong control over dissolution dynamics.

These findings also carried important implications for continuum-scale modeling. In our simulations dissolution could eradicate heterogeneity in

conduit diameters (or apertures) but could not remove heterogeneity rooted in pathway lengths and network connectivity; as a result, flow never became fully uniform in the disordered lattice or in the DFN. Darcy-scale finite-difference models, however, represent the medium only through spatially varying porosity or permeability fields. Because those fields evolve toward uniform values when diameters enlarge uniformly, such models would predict nearly complete flow homogenization under uniform dissolution—an outcome that, according to our network results, is unattainable in natural media where connectivity and length distributions persist. Capturing the true limits of homogenization will therefore require numerical approaches that retain at least some information on network topology, for example through higher-order upscaling techniques or hybrid continuum–network formulations.

5. Data Availability

All simulation data files are available in [75]. The software for dissolution and flow focusing profile calculation is provided in [76].

6. Acknowledgements

Research of J. D. Hyman and P. K. Kang was supported as part of the Center on Geo-process in Mineral Carbon Storage, an Energy Frontier Research Center funded by the U.S. Department of Energy, Office of Science, Basic Energy Sciences at the University of Minnesota under award #DE-SC0023429. Research of T. Szawęło and P. Szymczak was supported by the National Science Centre (NCN; Poland) under research Grant 2022/47/B/ST3/03395. Research of J. D. Hyman was also partially supported by CUSSP (Center for Understanding Subsurface Signals and Permeability), funded by the U.S. Department of Energy (DOE), Office of Science under FWP 81834. Los Alamos National Laboratory is operated by Triad National Security, LLC, for the National Nuclear Security Administration of U.S. Department of Energy (Contract No. 89233218CNA000001). LANL unclassified release number LA-UR-25-26376.

Appendix A. DFN Generation

We generate three-dimensional discrete fracture networks (DFN) using the DFNWORKS [54] software suite. The cornerstone of the DFN methodology, is that fractures tend to have a radius (length) that is much larger

than their aperture (height). This disparity is used to justify a co-dimension one representation of each fracture. For example, each fracture is a one-dimensional line in a two-dimensional simulation or a two-dimensional plane in a three-dimensional simulation. Thus, in our 3D DFN model, each fracture is represented as a rectangle using the methods described in [77]. These planes intersect with one another to form a network, through which flow and transport is simulated. The size, shape, orientation, and other hydrological properties are sampled from distributions whose parameters are determined from a site characterization, cf. [78] for a comprehensive discussion of DFN modeling approaches. Thus, `DFNWORKS` stochastically generates three-dimensional DFNs with desired characteristics such as length distributions and fracture intensities. Details of `DFNWORKS` in terms of algorithms and various applications can be found in [54].

We consider a semi-generic DFN loosely based on the fractured carbonate-hosted Pietrasecca Fault in the central Apennines, Italy, cf. [69] for detailed information about the fractured media. The domain is 25 m \times 10 m \times 10 m. We adopt three families from the survey and modify a few of their properties for our semi-generic study. Generation parameters of the networks are provided in Table A.1. We measure network surface area in terms of the fracture intensity [m^{-1}], which is the sum of surface area of each fracture (S_f) divided by the volume of the domain,

$$P_{32} = \frac{1}{V} \sum_f S_f. \quad (\text{A.1})$$

The fracture radii of all three families are sampled from a truncated power-law distribution with decay exponent α , minimum radius r_0 , and maximum radius r_u , and probability density function

$$p_r(r, r_0, r_u) = \frac{\alpha}{r_0} \frac{(r/r_0)^{-1-\alpha}}{1 - (r_u/r_0)^{-\alpha}}. \quad (\text{A.2})$$

We modify the minimum and maximum fracture radius from the data provided in [69]. This modification requires a change in the values of fracture intensity P_{32} . Fracture family orientations are sampled from a three dimensional von Mises Fisher distribution,

$$f(\mathbf{x}; \boldsymbol{\mu}, \kappa) = \frac{\kappa \exp(\kappa \boldsymbol{\mu}^T \mathbf{x})}{4\pi \sinh(\kappa)}. \quad (\text{A.3})$$

Discrete Fracture Network Families			
Parameter	Family #1	Family #2	Family #3
Aspect ratio	2	2	2
P_{32} [m ⁻¹]	2.52	4.84	0.315
Aperture [m]	2.23×10^{-6}	9.02×10^{-6}	3.67×10^{-6}
α	2.16	1.31	2.31
r_0 [m]	1	1	1
r_u [m]	5	5	5
κ	39.9	61.3	4.72
Trend [°]	330	337	263
Plunge [°]	86	87	51

Table A.1: Discrete Fracture Network parameters used for generating various fracture families.

In (A.3), $\boldsymbol{\mu}$ is the mean direction vector of the fracture family, T denotes transpose, and $\kappa \geq 0$ is the concentration parameter that determines the degree of clustering around the mean direction. Values of κ close to zero lead to a uniform distribution of points on the sphere while larger values create points with a small deviation from mean direction. To obtain uniformly random orientations, we set $\kappa = 0.1$ and mean normal vector of $(0, 0, 1)$. The distribution is sampled using the method detailed in [79].

Fractures from each family are placed into the domain with equal probability until the target P_{32} values are attained. After the network is generated, isolated fractures and clusters of fractures, those that do not connect inflow and outflow boundaries, are removed because they do not participate in flow and transport. We generate thirty independent and statistically identical networks.

Appendix A.1. Graph Representation

Once the networks are generated, we derive a graph / pipe-network representation using the method presented in [70]. At the core of the DFN methodology is the conceptual model of a set of fractures, which are discrete entities intersecting with one another to form a network. The following maps a DFN \mathcal{F} made up of a set of n fractures $\{f_i\}$ to a graph \mathcal{G} composed of a set of vertices V and edges E . If two fractures f_i and f_j intersect, $f_i \cap f_j \neq \emptyset$, then there is a vertex $v \in V$,

$$\psi : f_i \cap f_j \rightarrow v. \quad (\text{A.4})$$

that represents the line of intersection between the fractures f_i and f_j . If $f_i \cap f_j \neq \emptyset$ and $f_i \cap f_k \neq \emptyset$, then there is an edge in E connecting the corresponding vertices,

$$\psi : f_i \cap f_j \neq \emptyset \text{ and } f_i \cap f_k \neq \emptyset \rightarrow e(u, v) \in E. \quad (\text{A.5})$$

Under the mapping ψ each fracture is represented by a k -clique where k is the number of intersections on the fracture. Thus, each edge can be thought of as residing on a single fracture and edge weights can represent hydrological and geometric properties of that fracture.

References

- [1] C.-F. Tsang, I. Neretnieks, Y. Tsang, Hydrologic issues associated with nuclear waste repositories, *Water Resour Res* 51 (9) (2015) 6923–6972. doi:<https://doi.org/10.1002/2015WR017641>.
- [2] A. Churakov, W. Hummel, M. Fernandes, Fundamental research on radiochemistry of geological nuclear waste disposal, *CHIMIA* 74 (12) (2020) 1000–1009. doi:<https://doi.org/10.2533/chimia.2020.1000>.
- [3] A. E. Fryar, F. W. Schwartz, Hydraulic-conductivity reduction, reaction-front propagation, and preferential flow within a model reactive barrier, *J Contam Hydrol* 32 (3) (1998) 333–351. doi:[https://doi.org/10.1016/S0169-7722\(98\)00057-6](https://doi.org/10.1016/S0169-7722(98)00057-6).
- [4] K.-J. S. Kung, T. S. Steenhuis, E. J. Kladvivko, T. J. Gish, G. Bubenzer, C. S. Helling, Impact of preferential flow on the transport of adsorbing and non-adsorbing tracers, *Soil Sci Soc Am J* 64 (4) (2000) 1290–1296. doi:<https://doi.org/10.2136/sssaj2000.6441290x>.
- [5] K. U. Mayer, D. W. Blowes, E. O. Frind, Reactive transport modeling of an in situ reactive barrier for the treatment of hexavalent chromium and trichloroethylene in groundwater, *Water Resour Res* 37 (12) (2001) 3091–3103. doi:<https://doi.org/10.1029/2001WR000234>.
- [6] B. Berkowitz, H. Scher, Theory of anomalous chemical transport in random fracture networks, *Phys Rev E* 57 (5) (1998) 5858–5869. doi:<https://doi.org/10.1103/PhysRevE.57.5858>.

- [7] P. K. Kang, M. Dentz, T. Le Borgne, R. Juanes, Anomalous transport on regular fracture networks: Impact of conductivity heterogeneity and mixing at fracture intersections, *Phys Rev E* 92 (2) (2015) 022148. doi:<https://doi.org/10.1103/PhysRevE.92.022148>.
- [8] J. D. Hyman, G. Aldrich, H. Viswanathan, N. Makedonska, S. Karra, Fracture size and transmissivity correlations: Implications for transport simulations in sparse three-dimensional discrete fracture networks following a truncated power law distribution of fracture size, *Water Resour Res* 52 (8) (2016) 6472–6489. doi:<https://doi.org/10.1002/2016WR018806>.
- [9] M. Andreani, L. Luquot, P. Gouze, M. Godard, E. Hoisé, B. Gibert, Experimental study of carbon sequestration reactions controlled by the percolation of CO₂-rich brine through peridotites, *Environ Sci Technol* 43 (4) (2009) 1226–1231. doi:<https://doi.org/10.1021/es8018429>.
- [10] J. M. Matter, P. B. Kelemen, Permanent storage of carbon dioxide in geological reservoirs by mineral carbonation, *Nature Geosci* 2 (12) (2009) 837–841. doi:<https://doi.org/10.1038/ngeo683>.
- [11] C. I. Steefel, S. Molins, D. Trebotich, Pore scale processes associated with subsurface CO₂ injection and sequestration, *Rev Mineral Geochem* 77 (2013) 259–303. doi:<https://doi.org/10.2138/rmg.2013.77.8>.
- [12] J. D. Hyman, J. Jiménez-Martínez, C. W. Gable, P. H. Stauffer, R. J. Pawar, Characterizing the impact of fractured caprock heterogeneity on supercritical CO₂ injection, *Transp Porous Med* 131 (3) (2020) 935–955. doi:<https://doi.org/10.1007/s11242-019-01372-1>.
- [13] H. Nisbet, G. Buscarnera, J. W. Carey, M. A. Chen, E. Detournay, H. Huang, J. D. Hyman, P. K. Kang, Q. Kang, J. F. Labuz, W. Li, J. Matter, C. W. Neil, G. Srinivasan, M. R. Sweeney, V. R. Voller, W. Yang, Y. Yang, H. S. Viswanathan, Carbon mineralization in fractured mafic and ultramafic rocks: A review, *Rev Geophys* 62 (4) (2024) e2023RG000815. doi:<https://doi.org/10.1029/2023RG000815>.
- [14] A. Budek, P. Szymczak, Channeling, clogging and permeability oscillations: Different macroscopic regimes in mineral replacement, *J Geophys Res Solid Earth* 130 (6) (2025) e2024JB031081. doi:<https://doi.org/10.1029/2024JB031081>.

- [15] J. Chadam, D. Hoff, E. Merino, P. Ortoleva, A. Sen, Reactive infiltration instabilities, *IMA J Appl Math* 36 (3) (1986) 207–221. doi:<https://doi.org/10.1093/imamat/36.3.207>.
- [16] G. Daccord, R. Lenormand, Fractal patterns from chemical dissolution, *Nature* 325 (6099) (1987) 41–43. doi:<https://doi.org/10.1038/325041a0>.
- [17] M. L. Hoefner, H. S. Fogler, Pore evolution and channel formation during flow and reaction in porous media, *AIChE J* 34 (1) (1988) 45–54. doi:<https://doi.org/10.1002/aic.690340107>.
- [18] F. Golfier, C. Zarcone, B. Bazin, R. Lenormand, D. Lasseux, M. Quintard, On the ability of a darcy-scale model to capture wormhole formation during the dissolution of a porous medium, *J Fluid Mech* 457 (2002) 213–254. doi:<https://doi.org/10.1017/S0022112002007735>.
- [19] S. Molins, D. Trebotich, L. Yang, J. B. Ajo-Franklin, T. J. Ligocki, C. Shen, C. I. Steefel, Pore-scale controls on calcite dissolution rates from flow-through laboratory and numerical experiments, *Environ Sci Technol* 48 (13) (2014) 7453–7460. doi:<https://doi.org/10.1021/es5013438>.
- [20] H. P. Menke, B. Bijeljic, M. G. Andrew, M. J. Blunt, Dynamic three-dimensional pore-scale imaging of reaction in a carbonate at reservoir conditions, *Environ Sci Technol* 49 (7) (2015) 4407–4414. doi:<https://doi.org/10.1021/es505789f>.
- [21] F. Dutka, V. Starchenko, F. Osselin, S. Magni, P. Szymczak, A. J. C. Ladd, Time-dependent shapes of a dissolving mineral grain: Comparisons of simulations with microfluidic experiments, *Chem Geol* 540 (2020) 119459. doi:<https://doi.org/10.1016/j.chemgeo.2019.119459>.
- [22] C. N. Fredd, H. S. Fogler, Influence of transport and reaction on wormhole formation in porous media, *AIChE J* 44 (9) (1998) 1933–1949. doi:<https://doi.org/10.1002/aic.690440902>.
- [23] M. Garcia-Rios, L. Luquot, J. M. Soler, J. Cama, The role of mineral heterogeneity on the hydrogeochemical response of two fractured reservoir rocks in contact with dissolved CO₂, *Appl Geochem* 84 (1) (2017) 202–217. doi:<https://doi.org/10.1016/j.apgeochem.2017.06.008>.

- [24] H. Ott, S. Oedai, Wormhole formation and compact dissolution in single- and two-phase CO₂-brine injections, *Geophys Res Lett* 42 (7) (2015) 2270–2276. doi:<https://doi.org/10.1002/2015GL063582>.
- [25] J. Snippe, S. Berg, K. Ganga, N. Brussee, R. Gdanski, Experimental and numerical investigation of wormholing during CO₂ storage and water alternating gas injection, *Int J Greenh Gas Control* 94 (2020) 102901. doi:<https://doi.org/10.1016/j.ijggc.2019.102901>.
- [26] M. P. Cooper, R. P. Sharma, S. Magni, T. P. Blach, A. P. Radlinski, K. Drabik, A. Tengattini, P. Szymczak, 4D tomography reveals a complex relationship between wormhole advancement and permeability variation in dissolving rocks, *Adv Water Resour* 175 (4) (2023) 104407. doi:<https://doi.org/10.1016/j.advwatres.2023.104407>.
- [27] M. K. R. Panga, M. Ziauddin, V. Balakotaiah, Two-scale continuum model for simulation of wormholes in carbonate acidization, *AIChE Journal* 51 (12) (2005) 3231–3248. doi:<https://doi.org/10.1002/aic.10574>.
- [28] P. Szymczak, A. J. C. Ladd, Wormhole formation in dissolving fractures, *J Geophys Res* 114 (B6) (2009) B06203. doi:<https://doi.org/10.1029/2008JB006122>.
- [29] Y. Hao, M. Smith, Y. Sholokhova, S. Carroll, CO₂-induced dissolution of low permeability carbonates. Part II: Numerical modeling of experiments, *Adv Water Resour* 62 (2013) 388–408. doi:<https://doi.org/10.1016/j.advwatres.2013.09.009>.
- [30] C. I. Steefel, C. A. J. Appelo, B. Arora, D. Jacques, T. Kalbacher, O. Kolditz, V. Lagneau, P. C. Lichtner, K. U. Mayer, J. C. L. Meeussen, S. Molins, D. Moulton, H. Shao, J. Šimůnek, N. Spycher, S. B. Yabusaki, G. T. Yeh, Reactive transport codes for subsurface environmental simulation, *Comput Geosci* 19 (3) (2015) 445–478. doi:<https://doi.org/10.1007/s10596-014-9443-x>.
- [31] A. Budek, P. Szymczak, Network models of dissolution of porous media, *Phys Rev E* 86 (5) (2012) 056318. doi:<https://doi.org/10.1103/PhysRevE.86.056318>.

- [32] H. P. Menke, J. Maes, S. Geiger, Channeling is a distinct class of dissolution in complex porous media, *Sci Rep* 13 (1) (2023) 11312. doi:<https://doi.org/10.1038/s41598-023-37725-6>.
- [33] C. E. Cohen, D. Ding, M. Quintard, B. Bazin, From pore scale to wellbore scale: Impact of geometry on wormhole growth in carbonate acidization, *Chem Eng Sci* 63 (12) (2008) 3088–3099. doi:<https://doi.org/10.1016/j.ces.2008.03.021>.
- [34] P. Ortoleva, J. Chadam, E. Merino, A. Sen, Geochemical self-organization II; the reactive-infiltration instability, *Am J Sci* 287 (10) (1987) 1008–1040. doi:<https://doi.org/10.2475/ajs.287.10.1008>.
- [35] D. McDuff, S. Jackson, C. Shuchart, D. Postl, Understanding wormholes in carbonates: Unprecedented experimental scale and 3D visualization, *J Pet Technol* 62 (10) (2010) 78–81. doi:<https://doi.org/10.2118/129329-JPT>.
- [36] R. Roded, E. Aharonov, R. Holtzman, P. Szymczak, Reactive flow and homogenization in anisotropic media, *Water Resour Res* 56 (12) (2020) e2020WR027518. doi:<https://doi.org/10.1029/2020WR027518>.
- [37] H. P. Menke, M. G. Andrew, M. J. Blunt, B. Bijeljic, Reservoir condition imaging of reactive transport in heterogeneous carbonates using fast synchrotron tomography—effect of initial pore structure and flow conditions, *Chem Geol* 428 (2016) 15–26. doi:<https://doi.org/10.1016/j.chemgeo.2016.02.030>.
- [38] J. Jang, G. A. Narsilio, J. C. Santamarina, Hydraulic conductivity in spatially varying media—a pore-scale investigation, *Geophys J Int* 184 (3) (2011) 1167–1179. doi:<https://doi.org/10.1111/j.1365-246X.2010.04893.x>.
- [39] T. Szawelło, J. D. Hyman, P. K. Kang, P. Szymczak, Quantifying dissolution dynamics in porous media using a spatial flow focusing profile, *Geophys Res Lett* 51 (20) (2024) e2024GL109940. doi:<https://doi.org/10.1029/2024GL109940>.
- [40] W. Dreybrodt, The role of dissolution kinetics in the development of karst aquifers in limestone: A model simulation of karst evolution, *J Geol* 98 (5) (1990) 639–655. doi:<https://doi.org/10.1086/629431>.

- [41] W. Dreybrodt, Principles of early development of karst conduits under natural and man-made conditions revealed by mathematical analysis of numerical models, *Water Resour Res* 32 (9) (1996) 2923–2935. doi:<https://doi.org/10.1029/96WR01332>.
- [42] W. Durham, W. Bourcier, E. Burton, Direct observation of reactive flow in a single fracture, *Water Resour Res* 37 (1) (2001) 1–12. doi:<https://doi.org/10.1029/2000WR900228>.
- [43] R. L. Detwiler, R. J. Glass, W. L. Bourcier, Experimental observations of fracture dissolution: The role of Peclet number on evolving aperture variability, *Geophys Res Lett* 30 (12) (2003) 1648. doi:<https://doi.org/10.1029/2003GL017396>.
- [44] L. Li, C. I. Steefel, L. Yang, Scale dependence of mineral dissolution rates within single pores and fractures, *Geochim Cosmochim Acta* 72 (2) (2008) 360–377. doi:<https://doi.org/10.1016/j.gca.2007.10.027>.
- [45] P. Szymczak, A. J. C. Ladd, Microscopic simulations of fracture dissolution, *Geophys Res Lett* 31 (23) (2004) L23606. doi:<https://doi.org/10.1029/2004GL021297>.
- [46] R. B. Hanna, H. Rajaram, Influence of aperture variability on dissolutional growth of fissures in karst formations, *Water Resour Res* 34 (11) (1998) 2843–2853. doi:<https://doi.org/10.1029/98WR01528>.
- [47] R. L. Detwiler, H. Rajaram, Predicting dissolution patterns in variable aperture fractures: Evaluation of an enhanced depth-averaged computational model, *Water Resour Res* 43 (4) (2007) W04403. doi:<https://doi.org/10.1029/2006WR005147>.
- [48] F. Gabrovšek, W. Dreybrodt, A model of the early evolution of karst aquifers in limestone in the dimensions of length and depth, *J Hydrol* 240 (3) (2001) 206–224. doi:[https://doi.org/10.1016/S0022-1694\(00\)00323-1](https://doi.org/10.1016/S0022-1694(00)00323-1).
- [49] W. Dreybrodt, F. Gabrovšek, D. Romanov, *Processes of Speleogenesis: A Modeling Approach*, ZRC Publishing, Ljubljana, Slovenia, 2005.
- [50] S. Li, Z. Kang, X.-T. Feng, Z. Pan, X. Huang, D. Zhang, Three-dimensional hydrochemical model for dissolutional growth of fractures

- in karst aquifers, *Water Resour Res* 56 (3) (2020) e2019WR025631. doi:<https://doi.org/10.1029/2019WR025631>.
- [51] C. Jiang, X. Wang, S. Pu, H. Jourde, Incipient karst generation in jointed layered carbonates: Insights from three-dimensional hydro-chemical simulations, *J Hydrol* 610 (2022) 127831. doi:<https://doi.org/10.1016/j.jhydrol.2022.127831>.
- [52] C. Jiang, X. Wang, S. Pu, H. Jourde, Karst genesis and wormhole formation in carbonate joint networks: A comparison between 3D and 2D modeling, *J Hydrol* 619 (2023) 129303. doi:<https://doi.org/10.1016/j.jhydrol.2023.129303>.
- [53] M. C. Cacas, E. Ledoux, G. de Marsily, B. Tillie, A. Barbreau, E. Durand, B. Feuga, P. Peaudecerf, Modeling fracture flow with a stochastic discrete fracture network: Calibration and validation: 1. The flow model, *Water Resour Res* 26 (3) (1990) 479–489. doi:<https://doi.org/10.1029/WR026i003p00479>.
- [54] J. D. Hyman, S. Karra, N. Makedonska, C. Gable, S. Painter, H. Viswanathan, DFNWORKS: A discrete fracture network framework for modeling subsurface flow and transport, *Comput Geosci* 84 (2015) 10–19. doi:<https://doi.org/10.1016/j.cageo.2015.08.001>.
- [55] A. Pachalieva, J. D. Hyman, D. O'Malley, G. Srinivasan, H. Viswanathan, Learning the factors controlling mineral dissolution in three-dimensional fracture networks: Applications in geologic carbon sequestration, *Front Environ Sci* 12 (2025) 1454295. doi:<https://doi.org/10.3389/fenvs.2024.1454295>.
- [56] W. Cheung, H. Rajaram, Dissolution finger growth in variable aperture fractures: Role of the tip-region flow field, *Geophys Res Lett* 29 (22) (2002) 2075. doi:<https://doi.org/10.1029/2002GL015196>.
- [57] N. Kalia, V. Balakotaiah, Effect of medium heterogeneities on reactive dissolution of carbonates, *Chemical Engineering Science* 64 (2009) 376–390. doi:<https://doi.org/10.1016/j.ces.2008.10.026>.
- [58] P. Maheshwari, R. R. Ratnakar, N. Kalia, V. Balakotaiah, 3-D simulation and analysis of reactive dissolution and wormhole for-

- mation in carbonate rocks, *Chem Eng Sci* 90 (2013) 258–274. doi:<https://doi.org/10.1016/j.ces.2012.12.032>.
- [59] P. Maheshwari, V. Balakotaiah, Comparison of carbonate HCl acidizing experiments with 3D simulations, *SPE Prod Oper* 28 (04) (2013) 402–413. doi:<https://doi.org/10.2118/164517-PA>.
- [60] V. K. Upadhyay, P. Szymczak, A. J. C. Ladd, Initial conditions or emergence: What determines dissolution patterns in rough fractures?, *J Geophys Res Solid Earth* 120 (9) (2015) 6102–6121. doi:<https://doi.org/10.1002/2015JB012233>.
- [61] J. Deng, R. P. Sharma, P. Szymczak, P. K. Kang, Anomalous transport in dissolving porous media: Transitions between Fickian and non-Fickian regimes, *Geophys Res Lett* 52 (15) (2025) e2025GL115940. doi:<https://doi.org/10.1029/2025GL115940>.
- [62] A. Saeibehrouzi, S. Abolfathi, P. Denissenko, R. Holtzman, Non-monotonic impact of erosion on solute dispersion in porous media, *Geophys Res Lett* 52 (4) (2025) e2024GL114312. doi:<https://doi.org/10.1029/2024GL114312>.
- [63] Y. Al-Khulaifi, Q. Lin, M. J. Blunt, B. Bijeljic, Pore-scale dissolution by CO₂ saturated brine in a multimineral carbonate at reservoir conditions: Impact of physical and chemical heterogeneity, *Water Resour Res* 55 (4) (2019) 3171–3193. doi:<https://doi.org/10.1029/2018WR024137>.
- [64] T. Li, M. LI, X. Jing, W. Xiao, Q. CUI, Influence mechanism of pore-scale anisotropy and pore distribution heterogeneity on permeability of porous media, *Pet Explor Dev* 46 (3) (2019) 594–604. doi:[https://doi.org/10.1016/S1876-3804\(19\)60039-X](https://doi.org/10.1016/S1876-3804(19)60039-X).
- [65] R. P. Sharma, J. Deng, P. K. Kang, P. Szymczak, Effects of mixing at pore intersections on large-scale dissolution patterns and solute transport, *Geophys Res Lett* 50 (21) (2023) e2023GL105183. doi:<https://doi.org/10.1029/2023GL105183>.
- [66] Z. Kanavas, J. Jiménez-Martínez, F. Miele, J. Nimmo, V. Morales, Flow heterogeneity controls dissolution dynamics in topologically complex rocks, *Geophys Res Lett* 52 (8) (2025) e2024GL114369. doi:<https://doi.org/10.1029/2024GL114369>.

- [67] M. Aliouache, H. Jourde, Influence of structural properties and connectivity of initial fracture network on incipient karst genesis, *J Hydrol* 640 (2024) 131684. doi:<https://doi.org/10.1016/j.jhydrol.2024.131684>.
- [68] J. D. Hyman, A. C. Murph, L. Boampong, A. Navarre-Sitchler, J. W. Carey, P. Stauffer, H. S. Viswanathan, Determining the dominant factors controlling mineralization in three-dimensional fracture networks, *Int J Greenh Gas Control* 139 (2024) 104265. doi:<https://doi.org/10.1016/j.ijggc.2024.104265>.
- [69] L. Smeraglia, M. Mercuri, S. Tavani, A. Pignalosa, M. Kettermann, A. Billi, E. Carminati, 3D discrete fracture network (DFN) models of damage zone fluid corridors within a reservoir-scale normal fault in carbonates: Multiscale approach using field data and UAV imagery, *Mar Pet Geol* 126 (2021) 104902. doi:<https://doi.org/10.1016/j.marpetgeo.2021.104902>.
- [70] J. D. Hyman, A. Hagberg, D. Osthus, S. Srinivasan, H. Viswanathan, G. Srinivasan, Identifying backbones in three-dimensional discrete fracture networks: A bipartite graph-based approach, *Multiscale Model Simul* 16 (4) (2018) 1948–1968. doi:<https://doi.org/10.1137/18M1180207>.
- [71] P. Szymczak, A. J. C. Ladd, Reactive-infiltration instabilities in rocks. Fracture dissolution, *J Fluid Mech* 702 (2012) 239–264. doi:<https://doi.org/10.1017/jfm.2012.174>.
- [72] A. Bejan, *Convection Heat Transfer*, John Wiley & Sons, New York, NY, 1984.
- [73] R. E. Hayes, S. T. Kolaczkowski, Mass and heat transfer effects in catalytic monolith reactors, *Chem Eng Sci* 49 (21) (1994) 3587–3599. doi:[https://doi.org/10.1016/0009-2509\(94\)00164-2](https://doi.org/10.1016/0009-2509(94)00164-2).
- [74] N. Gupta, V. Balakotaiah, Heat and mass transfer coefficients in catalytic monoliths, *Chem Eng Sci* 56 (16) (2001) 4771–4786. doi:[https://doi.org/10.1016/S0009-2509\(01\)00134-8](https://doi.org/10.1016/S0009-2509(01)00134-8).
- [75] T. Szawełło, J. D. Hyman, P. K. Kang, P. Szymczak, Structural barriers to complete homogenization and wormholing in

- dissolving porous and fractured rocks [dataset], Zenodo (2025). doi:<https://doi.org/10.5281/zenodo.15771707>.
- [76] T. Szawełło, [tomaszszawello/poreNetDP](https://github.com/tomaszszawello/poreNetDP) [computer software], Dissolution v1.1. Zenodo (2025). doi:<https://doi.org/10.5281/zenodo.15775623>.
- [77] J. D. Hyman, C. Gable, S. Painter, N. Makedonska, Conforming delaunay triangulation of stochastically generated three dimensional discrete fracture networks: A feature rejection algorithm for meshing strategy, *SIAM J Sci Comput* 36 (4) (2014) A1871–A1894. doi:<https://doi.org/10.1137/130942541>.
- [78] H. S. Viswanathan, J. Ajo-Franklin, J. T. Birkholzer, J. W. Carey, Y. Guglielmi, J. D. Hyman, S. Karra, L. J. Pyrak-Nolte, H. Rajaram, G. Srinivasan, D. M. Tartakovsky, From fluid flow to coupled processes in fractured rock: Recent advances and new frontiers, *Rev Geophys* 60 (1) (2022) e2021RG000744. doi:<https://doi.org/10.1029/2021RG000744>.
- [79] A. T. A. Wood, Simulation of the von Mises Fisher distribution, *Commun Stat Simul Comput* 23 (1) (1994) 157–164. doi:<https://doi.org/10.1080/03610919408813161>.